Perturbative momentum transport in MAST L-mode plasmas

IOP Publishing | International Atomic Energy Agency Nuclear Fusion

Nucl. Fusion **57** (2017) 056022 (14pp) https://doi.org/10.1088/1741-4326/aa6501

Perturbative momentum transport in MAST L-mode plasmas

W. Guttenfelder[1], A.R. Field[2], I. Lupelli[2], T. Tala[3], S.M. Kaye[1], Y. Ren[1] and W.M. Solomon[4]

[1] Princeton Plasma Physics Laboratory, Princeton, NJ 08543, United States of America
[2] CCFE, Culham Science Centre, Abingdon, Oxfordshire, OX14 3DB, United Kingdom
[3] VTT, PO Box 1000, FIN-02044 VTT, Espoo, Finland
[4] General Atomics, San Diego, CA 92186, United States of America

E-mail: wgutten@pppl.gov

Received 13 December 2016, revised 15 February 2017
Accepted for publication 7 March 2017
Published 28 March 2017

Abstract

Non-axisymmetric magnetic fields are used to perturbatively probe momentum transport physics in MAST L-mode plasmas. The low beta L-mode target was chosen to complement previous experiments conducted in high beta NSTX H-mode plasmas ($\beta_N = 3.5$–4.6) where an inward momentum pinch was measured. In those cases quasi-linear gyrokinetic simulations of unstable ballooning micro-instabilities predict weak or outward momentum convection, in contrast to the measurements. The weak pinch was predicted to be due to both electromagnetic effects at high beta and low aspect ratio minimizing the symmetry-breaking of the instabilities responsible for momentum transport. In an attempt to lessen these electromagnetic effects at low aspect ratio, perturbative experiments were run in MAST L-mode discharges at lower beta ($\beta_N = 2$). The perturbative transport analysis used the time-dependent response following the termination of applied 3D fields that briefly brake the plasma rotation (similar to the NSTX H-mode experiments). Assuming time-invariant diffusive (χ_φ) and convective (V_φ) transport coefficients, an inward pinch is inferred with magnitudes, $(RV_\varphi/\chi_\varphi) = (-1)$–$(-9)$, similar to those found in NSTX H-modes and in conventional tokamaks. However, if experimental uncertainties due to non-stationary conditions during and after the applied 3D field are considered, a weak pinch or even outward convection is inferred, $(RV_\varphi/\chi_\varphi) = (-1)$–$(+5)$. Linear gyrokinetic simulations indicate that for these lower beta L-modes, the predicted momentum pinch is predicted to be relatively small, $(RV_\varphi/\chi_\varphi)_{sim} \approx -1$. While this falls within the experimentally inferred range, the uncertainties are practically too large to quantitatively validate the predictions. Challenges and implications for this particular experimental technique are discussed, as well as additional possible physical mechanisms that may be important in understanding momentum transport in these low aspect ratio plasmas.

Keywords: momentum transport, gyrokinetics, spherical tokamaks

(Some figures may appear in colour only in the online journal)

1. Introduction

Strong toroidal rotation and rotation shear can improve both macroscopic stability and confinement in tokamaks. In addition to torque sources and sinks, it is therefore important to understand the transport mechanisms that determine the toroidal rotation profile in order to develop predictions for future devices such as ITER [1]. The transport of toroidal angular momentum $L = nm\langle R^2\rangle\Omega$ is often written as a sum of three general parts [2, 3],

$$\Pi_\varphi = nm\langle R^2\rangle\,[-\chi_\varphi \nabla\,\Omega + (V_\varphi + \Gamma_n/n)\Omega] + \Pi_{\varphi,RS}, \quad (1)$$

where n is the ion density, m is the ion mass, R is major radius, $\langle\ldots\rangle$ represents the flux surface average, and Ω is the toroidal angular rotation. In addition to outward diffusion

(χ_φ), proportional to the rotation gradient, there is a convective contribution proportional to rotation itself (including a momentum specific convection V_φ and regular particle convection Γ_n). There can also be 'residual stress' contributions ($\Pi_{\varphi,\mathrm{RS}}$) not explicitly dependent on rotation or rotation gradient, which can also be thought of as the source of intrinsic torque, $T_{\mathrm{int}} = -\nabla \cdot \Pi_{\varphi,\mathrm{RS}}$ [4]. The diffusive component is typically characterized by the Prandtl number $\mathrm{Pr} = \chi_\varphi/\chi_\mathrm{i}$, the ratio of momentum to ion thermal diffusivity, which is order unity as expected from turbulence theory [5]. Ignoring the residual stress term, multiple tokamak experiments, using perturbative methods, have inferred the presence of a momentum pinch [6], with a normalized pinch parameter RV_φ/χ_φ ranging between -1 and -10. In many cases the pinch can be explained by the Coriolis drift mechanism [7–12], with relatively good quantitative agreement found between experiment and theory predictions based on local, quasi-linear gyrokinetic calculations of the ion temperature gradient (ITG) instability [13–15].

Additional work has extended the investigation of momentum pinch from conventional aspect ratio tokamaks ($R/a \sim 3$) to lower aspect ratio ($R/a \sim 1.5$) spherical tokamak (ST) plasmas and found discrepancy between the measured and predicted momentum pinch. Previous perturbative measurements in low aspect ratio NSTX H-modes have indicated the existence of an inward momentum pinch with a magnitude similar to that observed in conventional aspect ratio tokamaks, $RV_\varphi/\chi_\varphi = (-1)$–$(-7)$ [16–18]. However, local, linear gyrokinetic simulations run for these cases [19] predict the microtearing mode is the dominant micro-instability in the region of interest ($\rho = 0.5$–0.7) due to the relatively large plasma beta ($\beta_\mathrm{T} = 12$–16%, $\beta_\mathrm{N} = 3.5$–4.6) [20]. While microtearing turbulence provides negligible momentum transport (compared to electron thermal transport [21–24]), in these discharges a variety of weaker yet unstable ballooning modes are also predicted at lower wavenumbers ($k_\theta \rho_\mathrm{s}$) including ITG, compressional ballooning modes (CBM, which depend explicitly on the presence of compressional magnetic perturbations at high beta), and kinetic ballooning modes (KBM). Quasi-linear calculations were used to predict the momentum pinch from these sub-dominant ballooning modes, assuming they contribute substantially to the momentum transport. In all cases investigated the predicted pinch number is small or directed outward ($RV_\varphi/\chi_\varphi \geqslant 0$) for all of the ballooning modes (ITG, KBM, CBM) in contradiction to the experimental results. Additional scans show that the weak pinch is a consequence of how both electromagnetic effects (at relatively high beta) and low aspect ratio constrain the symmetry-breaking of the instabilities that is responsible for the momentum transport [2].

Additional simulations for a low beta NSTX L-mode (for which no perturbative data is available), unstable to more traditional electrostatic ITG-TEM instability, indicate an inward pinch that was also relatively weak, $RV_\varphi/\chi_\varphi \sim (-1)$–$(-2)$, and insensitive to variation in most parameters investigated. However, two cases were identified where a larger inward pinch was recovered. First, if the trapped particle fraction is decreased (either by reducing r/a or increasing aspect ratio R/a), a stronger inward pinch can be recovered, although this effect is non-monotonic. Second, in the purely electrostatic limit ($\beta \to 0$), a scaling with density gradient similar to that measured and predicted in conventional tokamaks [7, 13–15] is predicted, $RV_\varphi/\chi_\varphi \sim -0.5R/L_n$.

To provide an additional experimental test of momentum pinch theory at low aspect ratio while attempting to minimize electromagnetic effects, experiments were performed in MAST L-mode plasmas to reach beta values ($\beta = 4\%$, $\beta_\mathrm{N} = 2$) smaller than those in the NSTX H-modes. These experiments, motivated by an International Tokamak Physics Activity (ITPA) effort to compare momentum pinch and its parametric dependencies across different tokamaks [15], were conducted during the final MAST campaign (2013).

The remainder of the paper is organized as follows. Section 2 summarizes the conditions and characteristics of the L-mode plasmas that are being investigated and illustrates the perturbative approached using applied 3D fields (following [16–18]). The influence of sawteeth on the plasma profiles is investigated through the use of conditional averaging. While the sawteeth measurably influence the rotation profile, the perturbations are weaker and faster than that due to the applied 3D fields and are therefore filtered out for the perturbative transport analysis. Section 3 then presents the inferred momentum transport coefficients using the time-dependent rotation response after the applied 3D field is removed (no NTV torque). The presence of an inward pinch with a strength $RV_\varphi/\chi_\varphi \approx (-1)$–$(-9)$ is inferred around the mid-radius, assuming transport coefficients constant in time (χ_φ, $V_\varphi \sim$ constant). However, in these discharges the energy confinement and local thermal diffusivities vary ~20% during and after the applied 3D field (i.e. not an ideal perturbative experiment). If the momentum transport coefficients are assumed to be proportional to this variation (i.e. constant $\mathrm{Pr} = \chi_\varphi/\chi_\mathrm{i}$ and pinch parameter RV_φ/χ_φ), the inferred pinch is near zero and even outward in some locations $RV_\varphi/\chi_\varphi \approx (-1)$–$(+5)$. Results from linear gyrokinetic simulations are shown section 4, where a weak pinch $(RV_\varphi/\chi_\varphi)_\mathrm{sim} \approx -1$ is predicted from the ITG instability. Electromagnetic microtearing modes are also unstable, illustrating that the discharges are at sufficiently high beta to drive fundamentally electromagnetic instability, and therefore it is not surprising that the predicted pinch is weak. While the predicted weak pinch falls within the experimentally inferred range, the uncertainties are practically too large to quantitatively validate the predictions. Additional possible physical mechanisms that may be important in understanding momentum transport in these low aspect ratio plasmas are also discussed. Section 5 summarizes the results.

2. Experimental discharges

The MAST discharges under investigation are lower-single-null (LSN) diverted L-mode plasmas with a toroidal magnetic field $B_\mathrm{T} = 0.5$ T, plasma current of $I_\mathrm{p} = 400$ kA, line-averaged

density $\langle n_e \rangle \approx 2.3 \times 10^{19}$ m^{-3} and NBI heating power $P_{NBI} = 2$ MW using one co-I_p directed beam injector. The plasmas exhibit sawteeth, which will be discussed further below. Short $n = 3$ magnetic perturbations (20 ms ramp-up, 40 ms flattop, 20 ms ramp-down; 1.4 kA or 5.6 kA-turn) were applied to briefly perturb the plasma rotation, so that the transient response can be used to infer χ_φ and V_φ (discussed in section 3).

Time-traces of relevant parameters for three 400 kA L-modes are shown in figure 1 including I_p, P_{NBI}, line-integrated density ($n_e \cdot L$), stored energy, β_N, a lower-divertor D_α signal, and $n = 3$ coil current. Shots 29890 and 29892 are repeat shots that have three $n = 3$ pulses, while shot 29891 is a reference shot with no applied $n = 3$ field. During the plasma current flat-top, after $t > 300$ ms the density reaches a stationary state. With the application of $n = 3$ fields ($t = 0.33$–0.41 s) there is a small but noticeable density pump out ($\Delta n/n \sim 5\%$), as observed previously in MAST L-mode using even parity $n = 3$ perturbations [25]. There is a corresponding ~20% drop in stored energy and beta. In the baseline discharge without $n = 3$ fields an L-H mode transition eventually occurs at $t = 470$ ms. This is consistent with the previously observed delay or suppression of L-H transition in MAST plasmas using $n = 1$, 2, and 3 field perturbations [26]. The analysis in the remainder of the paper focuses on the time-window between $t = 0.3$–0.45 s, which includes just before, during, and after the second $n = 3$ field pulse when all three discharges remain in L-mode.

Before continuing we note that similar L-mode plasmas were run at $I_p = 600$ kA, with and without $n = 3$ fields, to provide a second plasma condition to investigate the perturbed momentum transport. However, these discharges transitioned to H-mode too early to provide a sufficient time window for momentum pinch analysis.

To generate the rotation braking, the internal ELM control coils were utilized, which is composed of two rows of coils (6 in the upper row, 12 in the lower row) with four turns per coil [27]. To ensure sufficient rotation braking in the L-mode plasma using $n = 3$ fields, the plasma center was shifted down ~12 cm into a lower single null configuration to bring the plasma closer to the lower row of coils. Only the lower row of coils was energized with the following relative current direction in each coil: $++--++--++--$. The poloidal cross section of example flux surfaces and the location of the lower row of coils is shown in figure 2. The equilibria were determined using EFIT++ [28] constrained to magnetics measurements, the pressure profile and the magnetic pitch angle measured using the motional Stark effect (MSE) diagnostic [29]. Additional equilibrium parameters of interest are $q_{95} = 5.3$, $\beta_T = 4\%$, $\beta_N = 2$, $R = 0.88$ m and $a = 0.55$ m.

The 2D, axisymmetric equilibrium reconstructions are found to be very similar in both discharges with and without $n = 3$ fields applied. Figure 2 shows that the flux surfaces (evenly spaced in normalized poloidal flux, $\Delta\psi_N = 0.1$) at $t = 0.369$ s for both 29890 (with $n = 3$ field perturbation) and 29891 (without $n = 3$ perturbation) overlay almost exactly. At a later time in both discharges ($t = 0.432$ s, after the $n = 3$ field is turned off in 29890), the flux surfaces still show similar agreement, and are nearly identical to those at $t = 0.369$ s.

The strength of the nonaxisymmetric equilibrium components is predicted using the ideal perturbed equilibrium code (IPEC) [30] for the dominant $n = 3$ component. The perturbed field strength is largest at the edge with magnitude $\delta B/B \sim 10^{-3}$, and reduces moving in towards the core, as is typically expected. The plasma response to the applied $n = 3$ field is composed of significant non-resonant components ($m \neq nq$) and is substantially different from the vacuum response. The resulting 3D perturbations give rise to non-ambipolar neoclassical transport and a resulting torque due to neoclassical toroidal viscosity (NTV) which brakes the plasma rotation [31], and has been observed previously in MAST discharges with externally applied 3D fields [32].

Example profiles of electron density and temperature measured with Thomson scattering [33], and ion temperature and toroidal rotation (measured with charge exchange recombination spectroscopy, CXRS [34]) are shown in figure 3 for three time slices just before (~0.335 s), during (~0.395 s) and after (0.435 s) the second 3D pulse was applied in discharge 29890. There is a very clear change in the rotation profile due to the NTV rotation braking, and a recovery of the rotation after the $n = 3$ field is removed. The density pump-out is also visible in the n_e profile outside 1.2 m and the influence of sawteeth is apparent in the T_e profile inside 1.2 m.

To more clearly examine the NTV rotation braking, figure 4 shows the rotation evolution at a few spatial locations for the discharge with $n = 3$ fields (29890, black) and without (29891, red), measured by the 64 channel CXRS system with ~1 cm and 5 ms spatial and time resolution, respectively. The peak toroidal rotation rate is $\Omega \approx 75$ krad s^{-1}, which corresponds to $V_{tor} \approx 75$ km s^{-1} or a Mach number of $\mathrm{Ma} = v_{Tor}/c_s = 0.4$ (using $c_s = (T_e/m_d)^{1/2}$), and falls off to $\leqslant 5$ krad s^{-1} towards the plasma edge. The dashed line shows the raw CXRS data, where the small oscillations associated with the sawteeth are apparent. The sawteeth have an average period of 12 ms, so to help clarify the slower response of the rotation to the applied $n = 3$ field, a 3-point (15 ms) moving-average boxcar filter is applied as shown by the solid lines.

While the rotation is not completely stationary leading up to the energizing of the $n = 3$ field ($t = 0.33$ s), there is a clear response compared to the case without $n = 3$ fields. The response is seen first at radii $R = 120$–125 cm, but within 5–10 ms is seen across the entire minor radius from the edge in towards the magnetic axis. (We note that measurements are made at the midplane, $Z = 0$, and therefore cannot reach the axis due to the downward shifted equilibrium, $Z = -12$ cm, shown in figure 2). The magnitude of the perturbed toroidal angular rotation $\Delta\Omega$ ranges between 3 krad s^{-1} at the edge to 20 krad s^{-1} near the axis. After the turn-off of the $n = 3$ fields ($t = 0.41$ s), the rotation recovers and approaches the value of rotation for the reference shot for almost all radii except those nearest the magnetic axis. The braking of rotation during the initial application of the $n = 3$ field can be used to infer NTV

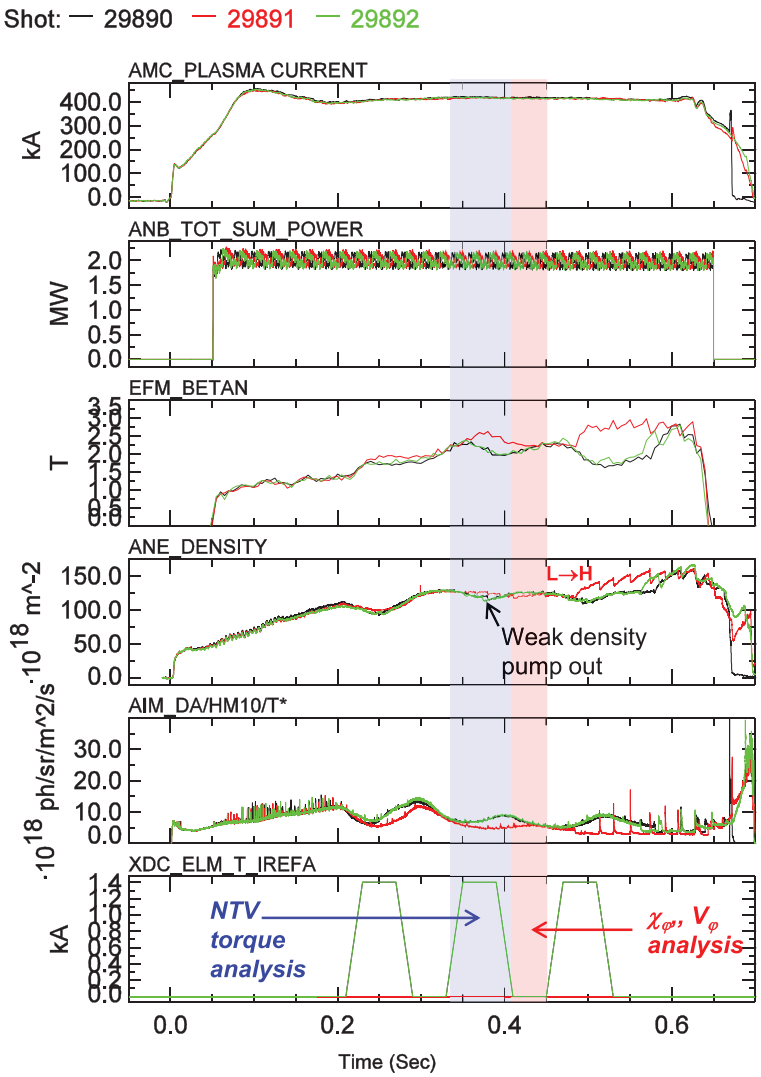

Figure 1. Time traces of plasma current, total injected beam power, normalized beta, line-averaged density, divertor *D*-alpha, and applied $n = 3$ current for three L-mode discharges. The regions shaded in blue and red are used to NTV torque and momentum transport, respectively.

torque. The response of the rotation after removal of the $n = 3$ field, where precise knowledge of the NTV torque is unnecessary and the torque from NBI heating can be accurately calculated, is used to infer χ_φ and V_φ, which will be discussed in section 3.

In the case of 29891 without applied 3D fields, there is also a background evolution in the rotation. A spectrogram of magnetic fluctuations measured by a Mirnov coil shows bursts of $n = 1$ and $n = 2$ perturbations that are associated with the sawteeth (figure 5), however there is no persistent low-frequency MHD activity apparent that could be the cause of the rotation response, such as NTV torque from the $n = 1$ 'long-lived mode' LLM [35, 36]. There are instances where some degree of inter-sawteeth activity is apparent. e.g. during the period $t = 0.37$–0.38 s between two sawteeth in shot 29891 there is some continuous activity at $f \sim 27$ and 55 kHz, however it is unclear whether this activity is related to the decrease in core rotation that begins around $t = 0.39$ s as seen in figure 4. While this generates some uncertainty in the following analysis, there still remains a clear difference in rotation without and with applied $n = 3$ fields that can be used to infer perturbative momentum transport. We also note that in discharge 29890, there is no change in magnetic fluctuation activity due to the energizing of the $n = 3$ fields ($t = 0.33$–0.41 s).

We now take a closer look at the extent over which sawteeth influence the plasma profiles. Figure 6 shows rotation data at multiple radii for shot 29890. The dashed vertical lines show the times of the sawtooth crashes as determined from a central chord soft x-ray measurement. While the slower time-scale evolution of rotation from the applied $n = 3$ field is apparent ($t = 0.33$–0.41 s), a change in rotation is also apparent around the times of the sawteeth. As the time-resolution of the CXRS

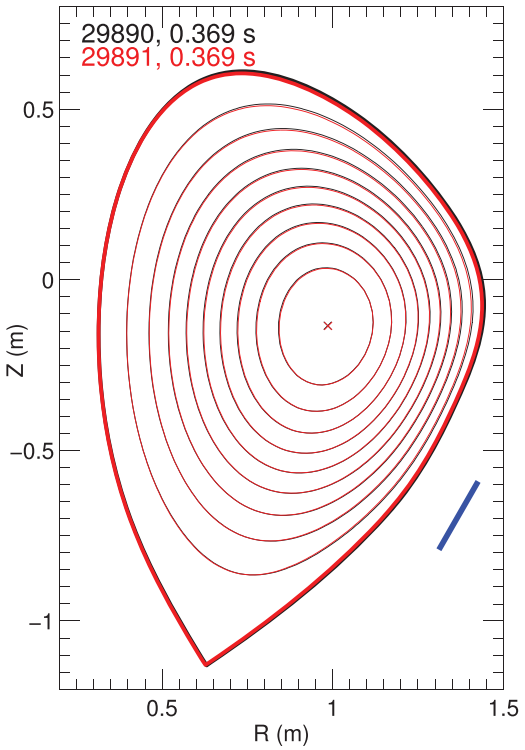

Figure 2. Flux surfaces from MSE-constrained EFIT++ (axisymmetric) reconstructions for two discharges with (29890, black) and without (29891, red) applied $n = 3$ fields. The straight blue line indicates the position of the lower 12 coils used to generate the $n = 3$ field.

measurement (5 ms) is far too slow to capture the fast transient response of the sawteeth, conditional averaging has been used to inspect how much the ensemble-averaged rotation changes using the two nearest measurements, before and after, each given sawtooth time. The same conditional averaging has been applied to the ion temperature measurements, as well as electron density and temperature from Thomson scattering (which have a time resolution of 4.2 ms).

Figure 7 shows the results of the conditional averaging using 12–14 sawteeth in each discharge in the 15 ms time window $t = 0.3$–0.45 s. The electron temperature near the magnetic axis ($R = 0.99$ m) drops $\Delta T_e = -120$ eV (16% of T_{e0}) after the sawtooth crash, and there is a modest increase +50 eV 15–20 cm away from the axis. The ion temperature shows a similar response with a −60 eV drop (6% of T_{i0}) at the axis and +20 eV increase 15–20 cm away. The inversion radius of ΔT_e and ΔT_i corresponds with the radius where the $q = 1$ surface from MSE-constrained EFIT++ reconstructions is predicted to occur ($R_{out,q=1} = 114$–118 cm), as indicated by the vertical blue dashed lines in figure 7. This inversion radius corresponds to a normalized poloidal flux of $\psi_N = 0.19$–0.26 as indicated by the q-profiles in figure 8, shown for four times in discharge 29890. In contrast to the temperatures, there is no obvious perturbation in the electron density as a result of the sawteeth (<3%) consistent with previous results [37].

The central rotation is reduced after sawteeth by $\Delta\Omega_{ST} = -6$ krad s^{-1} (~10% of Ω_0), with a very small increase +1–2 krad s^{-1} just outside the inversion radius. For comparison, the corresponding change in rotation due to the applied $n = 3$ field is about $\Delta\Omega_{n=3} = 12$–15 krad s^{-1} inside the inversion radius and 10–3 krad s^{-1} from the inversion radius to the edge. The average period of sawteeth ($\Delta t_{ST} = 12$ ms) is shorter than the time interval used for the perturbative momentum transport analysis (⩾30 ms). Furthermore, as we will see below the transport analysis is most useful outside the inversion radius where the amplitude of rotation change is much smaller than that due to the applied $n = 3$ fields. We therefore assume that the momentum transport analysis is valid using a time-filtered signal that eliminates the sawteeth effects on the rotation (as shown in figure 3).

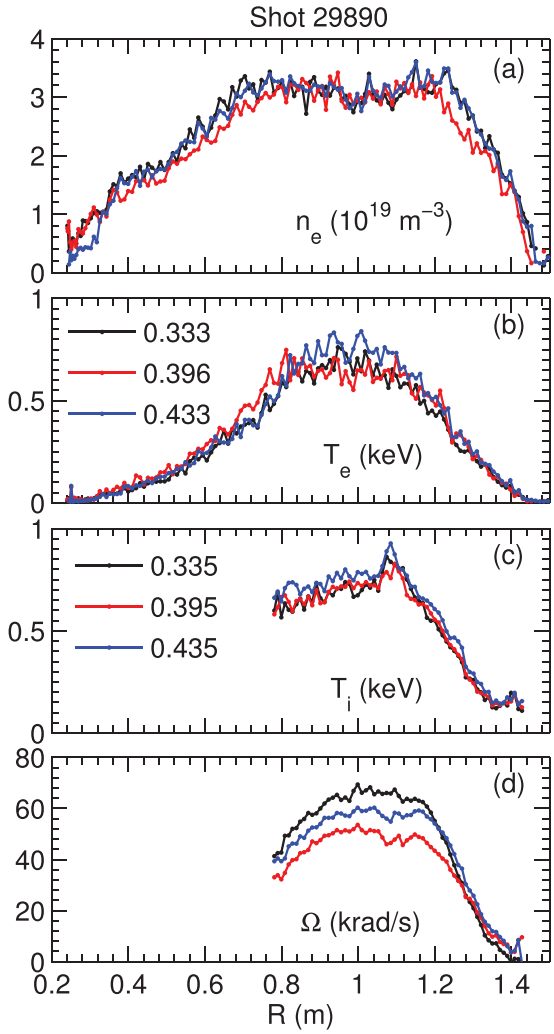

Figure 3. Radial profiles of electron density, electron temperature, ion temperature and toroidal rotation and three time slices just before, during and after the applied 3D fields in discharge 29890.

3. Momentum transport analysis

Transport analysis of the above discharges has been accomplished using the TRANSP code [38] coupled with NUBEAM [39] Monte Carlo calculations of the neutral beam sources and sinks. Following [40, 41], the flux-surface averaged, 1D

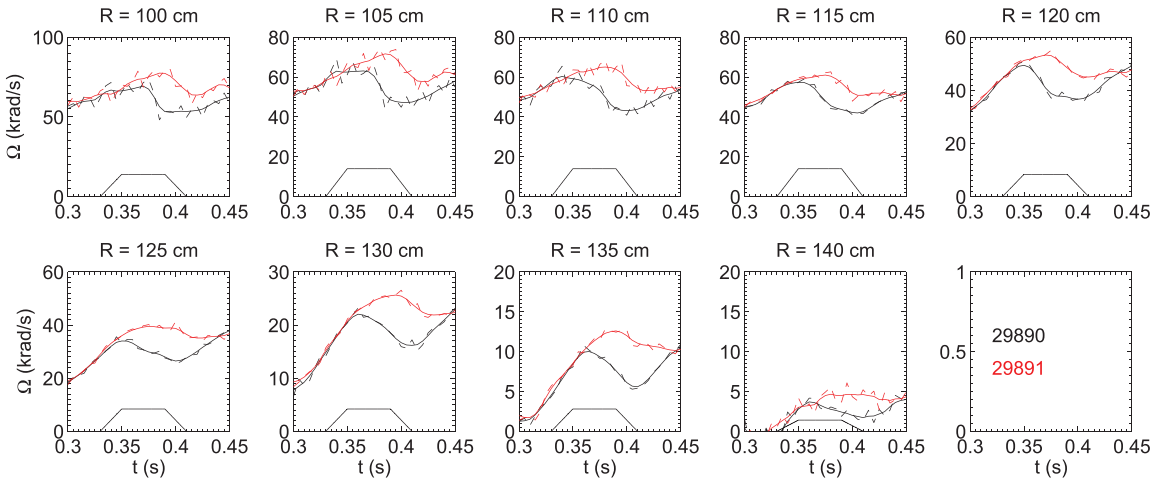

Figure 4. Time history of toroidal rotation at multiple radii in the two shots of figure 1. Dashed lines are the raw data, solid lines are the filtered signals. Waveform of the $n = 3$ field applied currents is also shown.

toroidal angular momentum equation solved by TRANSP is written as:

$$\frac{\partial}{\partial t}\left(\sum_i n_i m_i \langle R^2\rangle \Omega\right) + \frac{1}{V'}\frac{\partial}{\partial \rho}\left[V' \cdot \Pi_\varphi\right] = T_{\mathrm{NBI}} - T_{\mathrm{NTV}} \tag{2}$$

using the radial coordinate $\rho = (\Phi/\Phi_{\mathrm{LCFS}})^{1/2}$, where Φ is the toroidal flux, $V' = \mathrm{d}V/\mathrm{d}\rho$, and T_{NBI} represents the net torque source from NBI deposition, including $J \times B$ and collisional sources minus charge-exchange and ionization losses, all calculated by NUBEAM. T_{NTV} represents the sink due to NTV torque when the $n = 3$ coils are energized. Before turning to the profile analysis we first inspect the global confinement characteristics by volume integrating equation (2) to write a 0D evolution equation for the total plasma angular inertia, $L_{0\mathrm{D}}$, which depends on the volume-integrated net NBI torque, $T_{\mathrm{NBI,0D}}$, volume-integrated NTV torque, $T_{\mathrm{NVT,0D}}$, and global momentum confinement time, τ_φ:

$$\frac{\partial L_{0\mathrm{D}}}{\partial t} + \frac{L_{0\mathrm{D}}}{\tau_\varphi} = T_{\mathrm{NBI,0D}} - T_{\mathrm{NTV,0D}}. \tag{3}$$

Figure 9 shows the time evolution of $L_{0\mathrm{D}}$ in the two shots with and without $n = 3$ fields applied. The total angular momentum in the two shots is almost identical prior to the turn-on of the $n = 3$ field, and converges to the same value ~40 ms after the turn-off of the $n = 3$ field. Using the measured evolution of $L_{0\mathrm{D}}$ and the NBI torque calculated by TRANSP/NUBEAM, various fits have been performed to infer the global momentum confinement time and volume-averaged NTV torque from discharge 29890. Focusing first on the time after the removal of 3D fields (0.415–0.45 s, $T_{\mathrm{NTV}} = 0$), a momentum confinement time of $\tau_\varphi = 28$ ms is found, with a fit given by the blue line in figure 9. An additional fit over a wider time window that includes the period of applied 3D fields (0.36–0.45 s) was also performed assuming a NTV torque proportional to the square of the coil current, $T_{\mathrm{NTV}}(t) \sim I^2_{n=3}$ (green line in figure 9). The resulting fit gives a similar confinement time, $\tau_\varphi = 26$ ms, and volume-average NTV torque $T_{\mathrm{NTV}} = 0.28\,\mathrm{N}\cdot\mathrm{m}$. For comparison, the volume-integrated injected torque from NBI is $0.7\,\mathrm{N}\cdot\mathrm{m}$ and is peaked near-axis.

As discussed in section 2, the application of the 3D fields causes a ~20% reduction in energy confinement (figure 2). Therefore a third fit over the same time interval 0.36–0.45 s was performed assuming a momentum confinement time that follows the energy confinement time ($\tau_\varphi \sim \tau_{\mathrm{E}}$, red line). The resulting confinement time evaluated at 0.45 s (representative of the unperturbed value, long after the removal of the 3 D perturbation) remains very similar $\tau_\varphi = 28$ ms, with an improved quality of fit (χ^2_ν is reduced 70%). However, the resulting inferred NTV torque is reduced ~25%, $T_{\mathrm{NTV}} = 0.21\,\mathrm{N}\cdot\mathrm{m}$. We finally note that the momentum confinement times inferred from the various perturbative fits agree well with the momentum confinement time in the non-perturbed control discharge (29890), $\tau_{\varphi,\mathrm{control}} = 29$ ms with a statistical standard deviation of ± 3 ms over the time window of interest.

The inferred momentum confinement times are ~50% larger than the thermal energy confinement times of $\tau_{\mathrm{E,th}} = W_{\mathrm{th}}/(P_{\mathrm{abs}} + P_{\mathrm{OH}} - \mathrm{d}W/\mathrm{d}t) = 19$ and 17 ms for 29890 and 29891, respectively. This ratio of momentum to energy confinement, $\tau_\varphi/\tau_{\mathrm{E,th}} \sim 1.5$, is somewhat smaller than the ratio $\tau_\varphi/\tau_{\mathrm{E,th}} \sim 5$ inferred from the NSTX H-mode analysis [16, 17], possibly hinting at different relevant transport mechanisms controlling the plasma profiles. The NSTX H-modes were predicted to be unstable to electromagnetic microinstabilities that occur due to high beta, which are fundamentally different and unique compared to the traditional electrostatic ITG/TEM instabilities expected at lower beta and in conventional tokamaks. The near unity ratio of momentum to energy confinement in the MAST L-mode is similar to observations in conventional toakamaks ($\tau_\varphi \sim \tau_{\mathrm{E,th}}$), supporting this idea. Microstability analysis presented below will confirm that these discharges are in fact predicted to be unstable to electrostatic ITG modes, although weaker electromagnetic instabilities are also found which complicates the interpretation.

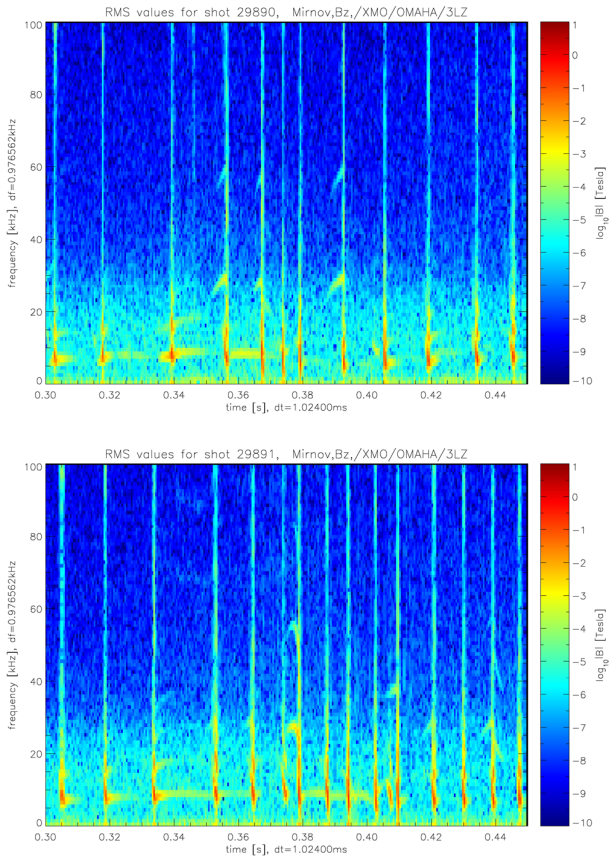

Figure 5. Magnetic spectrograms from a Mirnov coil for discharges (a) 29890 with applied stationary $n = 3$ perturbation, and (b) 29891, without $n = 3$ perturbation.

We now turn to the perturbative 1D analysis to infer momentum diffusivity and pinch profiles, using a 30 ms time period following the removal of the 3D fields ($T_{\mathrm{NTV}} = 0$) so the NTV torque profile does not need to be calculated or inferred. For this analysis we assume there is negligible residual stress in equation (1) so that $\prod_\varphi = nm\langle R^2\rangle(-\chi_\varphi \nabla \Omega + V_\varphi \Omega)$, where Π_φ is determine from TRANSP via equation (2). The solid data points in figures 10(*b*) and (*c*) show the resulting fit of χ_φ and V_φ, assuming they are constant in time. In this region the perturbative analysis indicates an inward directed momentum pinch with velocities between $V_\varphi = -5$ ms to -30 ms. The value of the inferred pinch is comparable to that found in NSTX H-modes. The momentum diffusivity $\chi_\varphi = 2$–3 m^2 s^{-1} is larger than the effective momentum diffusivity $\chi_{\varphi,\mathrm{eff}} \sim 1.8$ m^2 s^{-1} assuming purely diffusive transport ($V_\varphi = 0$).

Using the extra convective term gives a better quality of fit (χ^2_ν is reduced). However, in the middle of the analysis region ($\rho \sim 0.6$) the correlation between $\Omega(t)$ and $\nabla\Omega(t)$ is very strong (Pearson product $R > 0.9$) such that the solutions for χ_φ and V_φ become non-unique. As a result, the fit tends towards very large values of χ_φ and V_φ in this location (data points not shown). A strong $\Omega(t) - \nabla\Omega(t)$ correlation is also found outside the shown analysis region. However, there is no particularly strong variation in plasma profiles in this region, including the thermal diffusivities shown in figure 10(*a*), so we further assume that the transport coefficients should vary smoothly in radius. Instead of fitting the transport relationship for each radii independently, a parameterized form for the transport coefficients can be used to solve for the $\chi_\varphi(\rho)$ and $V_\varphi(\rho)$ profiles constrained using the entire analysis region ($\rho = 0.5$–0.7) simultaneously. This allows for a unique solution of $\chi_\varphi(\rho)$ and $V_\varphi(\rho)$ profiles even in the region where there is strong correlation between $\Omega(t)$ and $\nabla\Omega(t)$. Polynomial expansions up to 7th order were tried, with a best fit occurring using 2nd order. The resulting fit profiles of transport coefficients smoothly connect the values found in the single-radius fit procedure, as shown by the solid black lines in figures 10(*b*) and (*c*). The fit also give a smaller reduced χ^2_ν compared to the local fits, further justifying the approach.

For comparison, the ion and electron thermal diffusivities are shown in figure 10(*a*). As found in previous MAST transport analysis [42, 43], the electron thermal transport dominates the heat loss with $\chi_\mathrm{e} \approx 6$–$12$ m^2 s^{-1}. The experimentally inferred ion thermal diffusivity is about $2\times$ smaller, $\chi_\mathrm{i} \approx 2$–$5$ m^2 s^{-1}, and is comparable to the momentum diffusivities. The calculated neoclassical ion thermal diffusivity from NCLASS [44] is roughly constant over the analysis region, $\chi_{\mathrm{i,NC}} = 1.2$ m^2 s^{-1}, providing a significant fraction of the total ion transport near $\rho = 0.5$, but decreasingly less moving outward. The net anomalous $\chi_{\mathrm{i,anom}} = \chi_\mathrm{i} - \chi_{\mathrm{i,NC}}$ is shown in figure 10(*b*) and will be used below to calculate Prandtl numbers below.

In addition, as shown in figure 1 and discussed in the 0D analysis above, there is a ~20% reduction and recovery in stored energy during and after the applied 3D field perturbations. A similar variation is seen in the TRANSP-inferred thermal diffusivities, so it is natural to assume that the momentum transport coefficients might also follow this same trend. If the perturbative polynomial fitting procedure is applied assuming time-dependent $\chi_\varphi(\rho,t)$, $V_\varphi(\rho,t)$ that follow the ~20% variation in thermal diffusivities (effectively holding constant $\mathrm{Pr} = \chi_\varphi/\chi_\mathrm{i}$ and pinch parameter, RV_φ/χ_φ), smaller magnitudes of χ_φ and V_φ are inferred, given by the dashed lines in figures 10(*b*) and (*c*). While the reduction in diffusivity is roughly a factor of two, the momentum pinch is reduced significantly (in magnitude) to the point that it is near zero or outward directed over most of the analysis region (-1–$+5$ m s^{-1}). This adds considerable uncertainty in inferring the presence of a momentum pinch and to constraining the gyrokinetic predictions below. We note that no significant variation in energy confinement was observed in the NSTX H-mode experiments utilizing the 3D field perturbations, so this particular source of uncertainty did not appear in those discharges.

4. Linear gyrokinetic analysis

While nonlinear simulations are required to predict the magnitude of momentum transport, quasilinear calculations can be used to predict the relative ratio of transport contributions

such as Prandtl number $\mathrm{Pr} = \chi_\varphi/\chi_\mathrm{i}$ and momentum pinch parameter, RV_φ/χ_φ [2]. The GYRO code [45–47] has been used to predict microinstability in MAST discharge 29890 using a general representation [48] of the EFIT++ equilibrium reconstruction, kinetic electrons, kinetic deuterium and carbon ion species ($Z_\mathrm{eff} \approx 1.5$), pitch-angle scattering, and including fully electromagnetic perturbations (φ, $A_\parallel$, $B_\parallel$).

The linear simulations for this case predict that a broad spectrum of ITG modes are unstable at ion wavenumbers ($k_\theta \rho_\mathrm{s} < 1$) outside $\rho \geqslant 0.65$ as expected for a lower beta L-mode discharge (figures 11(*a*) and (*b*)). The ITG growth rates peak around $k_\theta \rho_\mathrm{s} = 0.4$ and become larger than the local $E \times B$ shearing rates (short dotted lines in figure 11(*b*)) moving outward in radius. Although nonlinear simulations have not been run, it is expected that the ITG turbulence will survive shear suppression in this region and contribute increasingly to the anomalous ion transport (figure 10(*b*)) and electron transport (figure 10(*a*)) that are also increasing with radius.

In addition to ITG there is also a spectrum of unstable microtearing modes (MTMs) at ion scales in the region of $\rho = 0.45$–0.6 (dashed lines in figures 11(*a*) and (*b*)). The MTM are distinguished from the ITG as they have tearing parity (odd-parity potential φ perturbations, even-parity shear magnetic $A_\parallel$ perturbations), strong magnetic fluctuation amplitudes $[(\delta A_\parallel/\rho_\mathrm{s} \cdot B_0)/(\mathrm{e}\delta\varphi/T_\mathrm{e}) \sim 1]$, and they propagate in the electron diamagnetic drift direction (positive real frequencies in figure 11(*a*)). The maximum MTM growth rates are very close to the $E \times B$ shearing rates, and may be expected to be supressed by $E \times B$ shear as found in nonlinear simulations based on NSTX discharges [21]. (We note that MTM simulations in conventional aspect ratio were much less sensitive to $E \times B$ shear suppressions [24].)

Microtearing modes are fundamentally electromagnetic in nature, requiring shear magnetic perturbations $\delta B_\perp = \nabla \times \delta A_\parallel$, and have been predicted previously in MAST H-modes at higher beta [49]. The presence of unstable MTM is somewhat unexpected in the L-mode plasmas at lower beta (a key motivation for running these discharges). However, in these spherical tokamak plasmas, volume-averaged beta is ~4% even in L-mode, and apparently large enough to destabilize EM microinstabilities which could possibly contribute to the significant electron thermal transport. We note that the ITG modes are fundamentally electrostatic in nature, and the growth rates increase a marginal ~15% in the purely electrostatic limit ($\beta_\mathrm{e} \to 0$).

In addition to ITG and MTM at ion scales, electron scale ($k_\theta \rho_\mathrm{s} \gg 1$) ETG instabilities are also unstable outside $\rho \geqslant 0.5$ (figures 11(*c*) and (*d*)) with growth rates increasing in radius. ETG turbulence can contribute substantially to electron thermal transport, and in cases where the $E \times B$ shearing rate is sufficiently large to suppress ion scale turbulence, electron-scale nonlinear simulations can be used to predict the amount of transport from ETG turbulence [50–52]. However, recent work has shown that multi-scale simulations are required to predict the correct transport when ion scale turbulence is near-marginal or above threshold [53], as in the cases here.

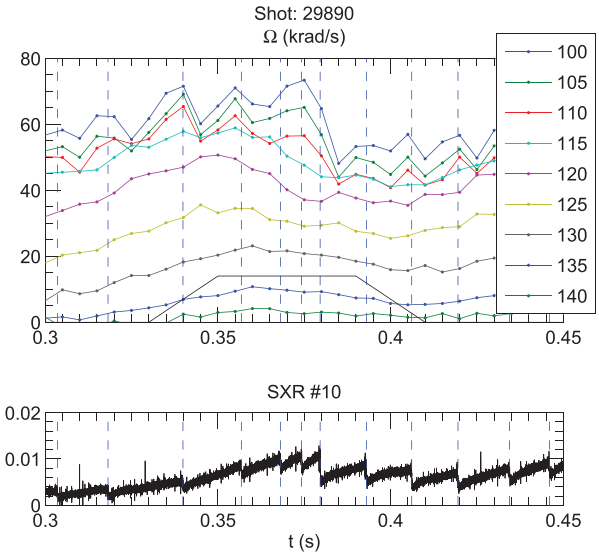

Figure 6. (top) Rotation time-series and different tangency radii (cm) and (bottom) soft x-ray measurement from central chord. Dashed lines represent the times of sawteeth.

Although the multiscale simulations are too expensive to run for these cases, neither MTM or ETG contribute to momentum transport. Of the unstable modes identified, only the ITG instability contributes significantly to the momentum transport. We therefore predict the quasilinear Pr and RV_φ/χ_φ parameters for the ITG instability where it is found to be unstable to compare with the experimental analysis in the previous section. To accomplish this, linear stability analysis was performed using combinations of $[u, u'] = [0, 0]$, $[1, 0]$, $[0, 1]$ $[1, 1]$, $\times$ $[u_\mathrm{exp}, u'_\mathrm{exp}]$, where $u = R\Omega/c_\mathrm{s}$ and $u' = -R^2\nabla\Omega/c_\mathrm{s}$, as has been discussed in previous publications (e.g. [2, 19]). While the growth rates are relatively insensitive to changes in u or u′, the difference in quasi-linear fluxes for different values of u or u′ can then be used to construct Pr ($\sim\Delta\Pi_\varphi/\Delta u'$) and RV_φ/χ_φ ($\sim\Delta\Pi_\varphi/\Delta u$). Note that the total momentum flux is composed of both deuterium and carbon ($\Pi_{\varphi,\mathrm{D}} + \Pi_{\varphi,\mathrm{C}}$), although the carbon contribution is negligible in these L-modes with small Z_eff.

Figure 12 shows the radial profile of the predicted Pr (figure 12(*a*)) and RV_φ/χ_φ (figure 12(*b*)), evaluated at $k_\theta \rho_\mathrm{s} = 0.4$ (near the maximum in growth rates). The corresponding profile of growth rates (ITG, MTM) and $E \times B$ shearing rates are shown in figure 12(*c*). As the mode-dominance between ITG and MTM varies radially, the GYRO eigenvalue solver [54] is used to track the instabilities. Over the region where ITG is unstable $\rho \geqslant 0.6$ the predicted $\mathrm{Pr}_\mathrm{sim} = 0.4$–$0.7$ and the pinch parameter is inward, constant and relatively weak, $(RV_\varphi/\chi_\varphi)_\mathrm{sim} = -1$. This weak predicted pinch is similar to that predicted for both NSTX H-mode and L-mode parameters [19].

For comparison to experiment, the experimental value of Prandtl and pinch parameters are shown in figure 12 using

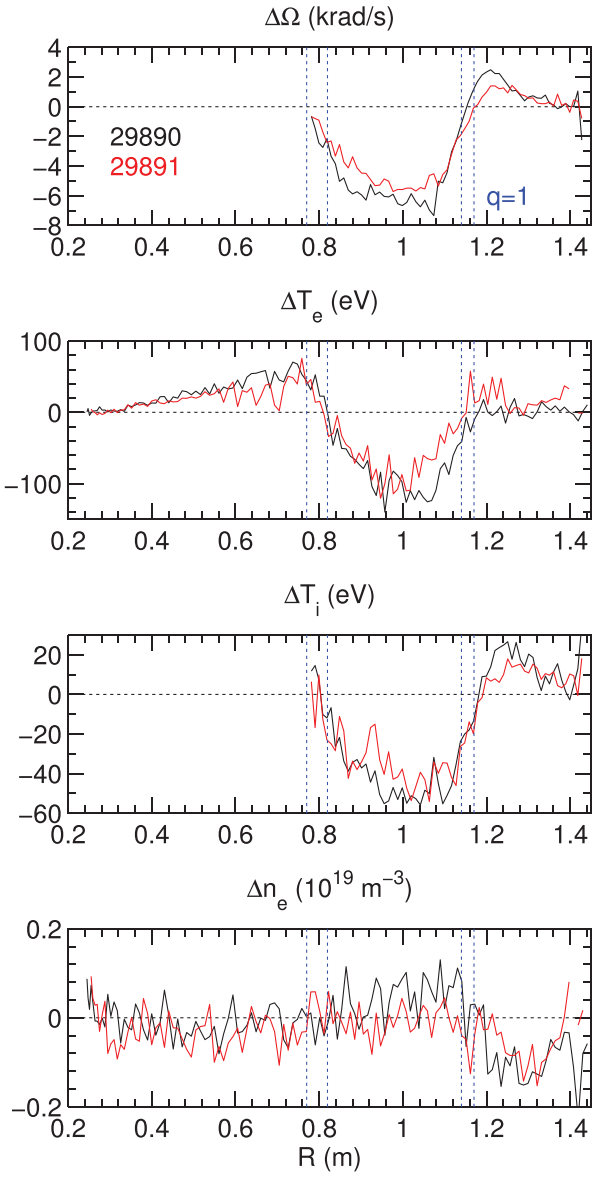

Figure 7. Average change in rotation, temperature and electron density conditionally averaged for time-slices before and after sawteeth.

the momentum diffusivities and pinch velocities inferred from the perturbative analysis above. The lines correspond to the same cases in figure 10 and the shaded region gives the bounds between the two fits that assume χ_φ, V_φ ~ constant (solid black) or time-dependent (dashed black). The Prandtl number is calculated using the anomalous ion thermal diffusivity, $\mathrm{Pr} = \chi_\varphi/\chi_{\mathrm{i,anom}}$, and gives a wide range of values, between $\mathrm{Pr} = 2$–3.5 at $\rho = 0.5$ where neoclassical transport dominates the ion thermal transport, and $\mathrm{Pr} = 0.6$–0.9 at $\rho = 0.7$ where the anomalous ion thermal contribution is dominant. Prandtl numbers significantly larger than unity are not predicted from theory and simulation, but experimentally is unavoidable in situations when the ion thermal transport

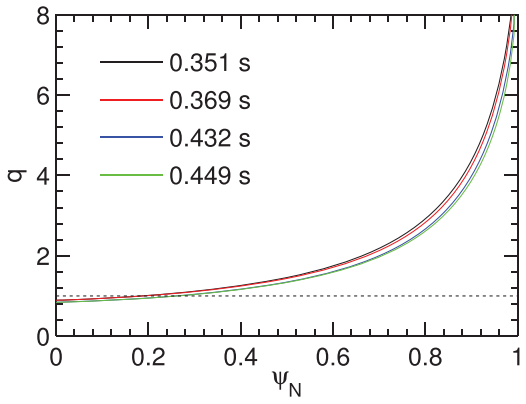

Figure 8. Profile of safety factor, q, versus normalized poloidal flux, ψ_N from EFIT++.

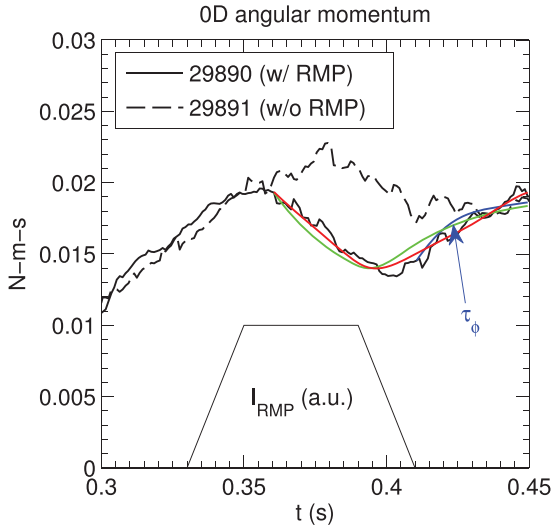

Figure 9. Time history of volume integrated angular momentum for shots without and with applied $n = 3$ perturbation. Also shown are the different fits to determine the global momentum confinement time and volume-averaged NTV torque.

approaches neoclassical levels ($\chi_{\mathrm{i,anom}} \to 0$) such as often found in spherical tokamaks. As electron losses dominate in these plasmas, an equivalent ratio of momentum to electron heat transport can instead be calculated, $\chi_\varphi/\chi_\mathrm{e}$, with values ranging between 0.15–0.3. Similar values of $\chi_\varphi/\chi_\mathrm{e} = 0.2$–$0.4$ have been predicted from quasilinear trapped electron mode (TEM) simulations [55], however TEM are not predicted in these MAST L-modes. It is conceivable that momentum transport from ITG coupled with electron heat transport from unstable MTM and ETG could account for the experimental ratios of $\chi_\varphi/\chi_\mathrm{i}$ and $\chi_\varphi/\chi_\mathrm{e}$, but this will require nonlinear, and possibly even multiscale, simulations.

The experimentally inferred pinch parameters are also shown in figure 12. For the constant coefficient analysis the pinch parameter varies between $RV_\varphi/\chi_\varphi = -1$ to -9. These values are very similar to those found in NSTX H-mode experiments [16–18] and also in conventional aspect ratio

tokamaks [6, 13–15]. However, the pinch parameter is much weaker or positive (outward), $RV_\varphi/\chi_\varphi = -1$ to $+5$, for the time-dependent coefficient fits. This wide uncertainty range of inferred pinch parameter is unfortunately too large to constrain the theoretical prediction.

Additional simulations in [19] showed that a larger inward pinch was recovered in the purely electrostatic limit with sufficient density gradient, similar to conventional tokamak results [7]. Additional scans show a similar result in this MAST L-mode case (figure 13), with an asymptotic dependence of $(RV_\varphi/\chi_\varphi)_{\rm sim} \sim -0.7 \cdot R/L_n$. However, the simulations at finite-β predict negligible pinch regardless of density gradient, indicating electromagnetic effects remain sufficiently strong to constrain mode-symmetry, minimizing any potential pinch contribution [19, 56].

Based on these simulations and similar previous simulations in NSTX, the predicted momentum pinch is expected to be largely insensitive to parameter variations. While the experimental uncertainties are too large in the present experiment to validate the predictions, there are other possible sources of momentum transport that could also influence the interpretation above. In particular there are a number of residual stress contributions that can add to momentum transport, grouped within $\Pi_{\rm RS}$ in equation (1).

As discussed in [2], the various physical mechanisms that cause momentum transport can be identified by how they break parallel and/or radial symmetry of the unstable modes. For example, while $E \times B$ shearing can suppress turbulent transport, it can also tilt eddies, breaking their radial and parallel symmetry thereby causing a momentum flux [57]. However, it was shown in nonlinear simulations [58] that this contribution becomes small for $E \times B$ shearing rates comparable to linear growth rates, which is similar to what is found in this MAST L-mode plasma (figure 12(*c*)).

Up-down flux surface asymmetry can also lead to a residual stress momentum flux [59, 60], which may be expected to contribute in the present case given the strong lower-biased equilibrium used (figure 2). The same set of linear simulations used to infer Pr and RV_j/χ_φ can also be used to infer the strength of this up-down asymmetry residual stress contribution, $\Pi_{\rm UD}$. To characterize this we normalize the momentum flux contributions in gyroBohm units as $\hat{\Pi}_\varphi = \hat{\chi}_\varphi [u' + (RV_\varphi/\chi_\varphi)u + \hat{C}_{\rm UD}/\hat{\chi}_\varphi]$ where $\hat{\Pi}_\varphi = \prod_\varphi/(\rho_s^2/R^2 \cdot n_{\rm ref} m_{\rm ref} R c_s)$, $\hat{\chi}_\varphi = \chi_\varphi/(\rho_s^2 c_s/R)$ and $\hat{C}_{\rm UD} = \Pi_{\rm UD}/(\rho_s^2/R^2 \cdot n_{\rm ref} m_{\rm ref} R c_s)$ represents the normalized residual stress from up-down asymmetry. Figure 14 shows the comparison of the diffusive component (u'), convective component ($RV_\varphi/\chi_\varphi \cdot u$) and the residual stress component ($\hat{C}_{\rm UD}/\hat{\chi}_\varphi$) in the MAST L-mode. The residual stress is inward directed over most of the radius, but relative to diffusion is even smaller than the already weak pinch. To verify this residual stress is in fact due to the up-down asymmetry, additional simulations were run removing the up-down asymmetric Fourier components in the equilibrium surface shape expansion [48]. The resulting predictions give zero residual stress and a very similar pinch contribution (dashed lines in figure 14).

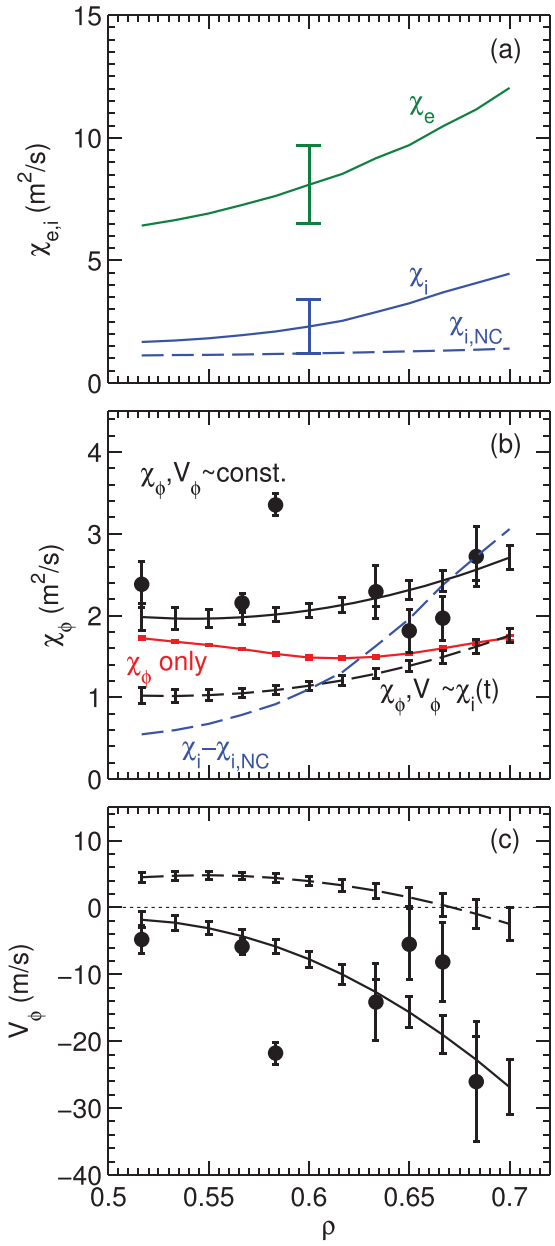

Figure 10. (*a*) Electron, ion and neoclassical ion thermal diffusivities. (*b*) Profiles of fit χ_φ assuming only diffusive transport (red) or diffusive and convective transport (black). The symbols are from the direct fit at each radii, while the lines assume a polynomial radial dependence that is constant in time (solid black) or time-dependent proportional to $\chi_i(t)$ (dashed black). Also shown is the anomalous ion thermal diffusivity, $\chi_i - \chi_{i,\rm NC}$ (blue dashed). (*c*) The corresponding profiles of the fit momentum convection coefficient, V_φ.

Recent gyrokinetic simulations for NSTX H-modes found that centrifugal effects can modify the momentum transport [61]. However, its relative contribution was found to be comparable in magnitude to the Coriolis pinch, which is much smaller than diffusion in this case as seen in figure 14.

There are also a number of finite-ρ^* effects that could lead to symmetry breaking and contribute to the momentum

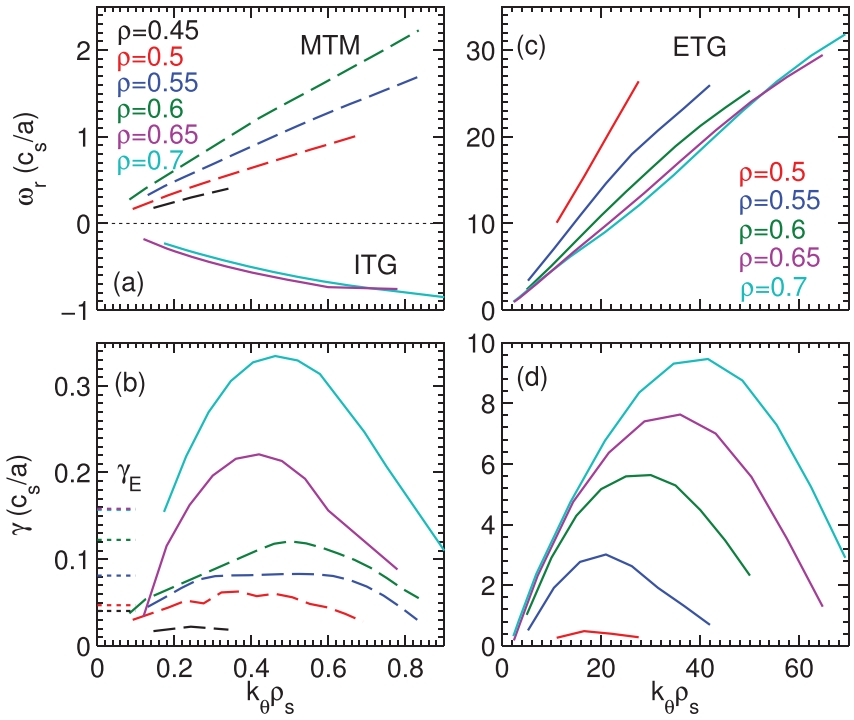

Figure 11. (*a*) and (*c*) Real frequencies and (*b*) and (*d*) linear growth rates versus normalized poloidal wavenumber calculated by GYRO simulations at different radii for (left) ion scales, $k_\theta\rho_s < 1$ and (right) electron scales, $k_\theta\rho_s > 1$. MTM and ETG real frequencies are in the electron diamagnetic drift direction ($\omega_r > 0$) while ITG are in the ion direction ($\omega_r < 0$). Short dotted lines in (*b*) show the local $E \times B$ shearing rates, γ_E.

flux, which could be important in the low-field strength spherical tokamak plasmas due to the relatively large values of $\rho^* = \rho_i/a \sim 1/B$. These effects include profile shearing of eddies due to radial variations in mode frequency (e.g. the variation of γ_{ITG} in figure 12(*c*) over a physical radial extent $L_r \approx 20\rho_s$) [62, 63], profile variation in the non-linear turbulence intensity [64], and zonal flow shearing [65, 66]. For reference, the MAST L-mode plasma investigated in this paper has $\rho^* = 1/85$ at the midradius. Nonlinear, global gyrokinetic simulations run in a previous MAST L-mode with $\rho^* = 1/55$ (and an internal transport barrier) [67, 68] showed that non-local effects can change the local quantitative transport and some turbulence spreading can occur. Similar simulations would be required to predict if finite-ρ^* turbulent residual stresses can contribute significantly to the momentum transport.

While it is challenging to infer residual stress contributions from plasmas with torque sources such as NBI heating, experiments in MAST ohmic L-mode and H-mode discharges with no external torque have observed intrinsic rotation as large as ~20–40 krad s^{-1} [69], which is a significant fraction of the rotation values in the MAST L-mode investigated in this paper. The intrinsic rotation in the ohmic plasmas reverses direction depending on collisionality, and was found to qualitatively agree with a model based on turbulent momentum flux associated with the non-Maxwellian neoclassical distribution [70, 71]. The model depends on finite orbit widths (at finite-ρ^*), density and temperature gradients, and collisionality. More specifically, the momentum transport is inward directed at collisionalities deep in the banana-plateau regime ($\nu^* < \varepsilon^{3/2}$, where $\nu^* = qR \cdot \nu_{ii}/\varepsilon^{3/2} \cdot v_{Ti}$), and outward directed far into the Pfirsch-Schleuter regime. In the MAST L-mode case the ions are in the banana-plateau regime over most of the minor radius ($\rho < 0.85$), so perhaps an inward directed momentum-flux contribution could be expected from this neoclassical effect. Future experiments will aim to further elucidate these various contributions to momentum transport in spherical tokamaks.

5. Summary

Non-axisymmetric magnetic fields are used to perturbatively probe momentum transport physics in MAST L-mode plasmas. The low beta L-mode target was chosen to complement previous experiments conducted in high beta NSTX H-mode plasmas ($\beta_N = 3.5$–4.6) where an inward momentum pinch was measured. In those cases quasi-linear gyrokinetic simulations of unstable ballooning micro-instabilities predict weak or outward momentum convection, in contrast to the measurements. The weak pinch was predicted to be due to both electromagnetic effects at high beta and low aspect ratio minimizing the symmetry-breaking of the instabilities responsible for momentum transport.

In an attempt to lessen these electromagnetic effects at low aspect ratio, perturbative experiments were run in MAST L-mode discharges at lower beta ($\beta_N = 2$). The analysis used the time-dependent response following the termination

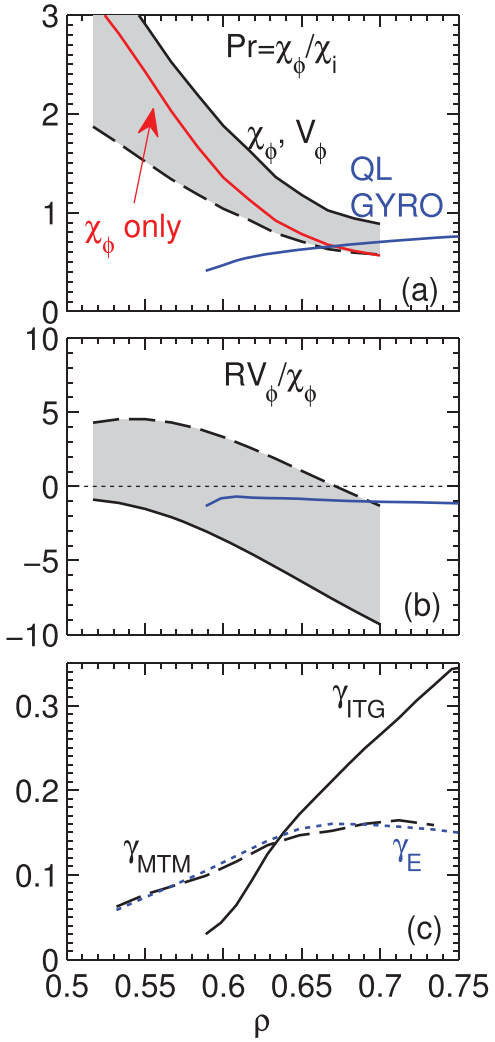

Figure 12. (*a*) Prandtl number χ_φ/χ_i from the various fits described in figure 10 including χ_φ only (red), χ_φ,V_φ constant (solid black line) and χ_φ,V_φ time-dependent (dashed black line). (*b*) Corresponding pinch parameter RV_φ/χ_φ. The blue lines show the predicted Pr and RV_φ/χ_φ from local, quasi-linear GYRO simulations of the ITG instability (evaluated at $k_\theta\rho_s = 0.4$ near the maximum growth rate). (*c*) Linear growth rates of ITG and MTM instability, and $E \times B$ shearing rate.

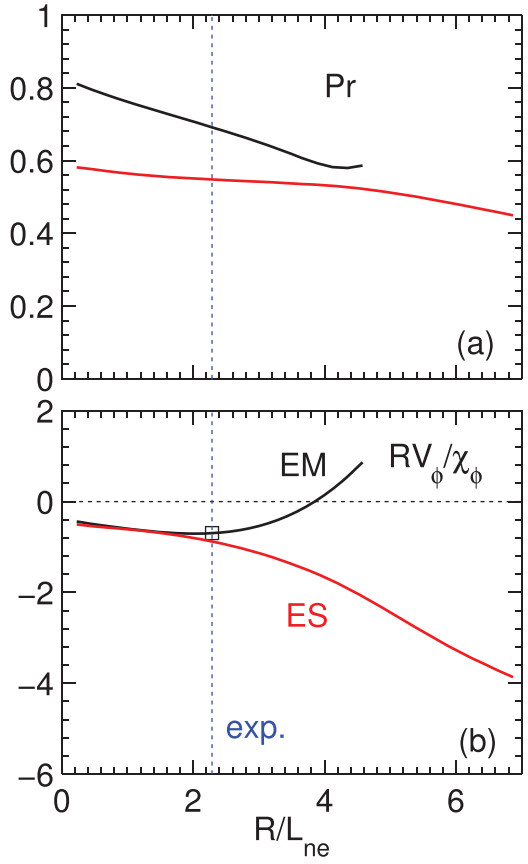

Figure 13. Predicted (*a*) Prandtl number and (*b*) pinch parameter RV_φ/χ_φ versus density gradient in the electromagnetic and electrostatic limit, evaluated for $\rho = 0.65$, $k_\theta\rho_s = 0.4$. The experimental value of density gradient is given by the dashed blue line.

of applied 3D fields that briefly brake the plasma rotation (similar to the NSTX H-mode experiments). Although these plasmas are sawtoothing, the influence on rotation is limited to inside the inversion radius ($\psi_N < 0.4$) and occurs on a time scale faster than transport so their influence on rotation have been filtered out. Assuming time-invariant diffusive (χ_φ) and convective (V_φ) transport coefficients, an inward pinch is inferred with magnitudes, $(RV_\varphi/\chi_\varphi) = (-1)$–$(-9)$, similar to those found in NSTX H-modes and in conventional tokamaks. However, if experimental uncertainties due to non-stationary conditions during and after the applied 3D field are considered, a weak pinch or even outward convection is inferred, $(RV_\varphi/\chi_\varphi) = (-1)$–$(+5)$. Linear gyrokinetic simulations indicate that for these lower beta L-modes, the predicted momentum pinch is relatively small, $(RV_\varphi/\chi_\varphi)_{sim} \approx -1$. Similar to predictions for NSTX, a larger pinch is predicted in the purely electrostatic case with increasing density gradient. However, the simulations at finite-β predict negligible pinch regardless of density gradient, indicating electromagnetic effects remain sufficiently strong to constrain mode-symmetry, minimizing any potential pinch contribution as discussed in earlier publications [19, 56]. In addition to the inconsistent pinch values, the measured Prandt numbers χ_φ/χ_i can be larger than predictions as the ion thermal diffusivities approach neoclassical levels. It remains unknown whether electron thermal transport can be accounted for by MTM and/or ETG instabilities while momentum transport by ITG. Nonlinear simulations will be required to predict self-consistent heat and momentum fluxes in plasmas like these.

Although the experimental uncertainties are too large to constrain the pinch predictions, additional theoretical contributions to the momentum flux are also considered which could influence the experimental interpretation. Most likely candidates are finite-ρ^* residual stress effects that could be amplified in the low field ST plasmas. Future experiments are planned on NSTX-U using long stationary L-mode plasmas [72] to further probe momentum transport and validate theory predictions at low aspect ratio using lower beta ST plasmas.

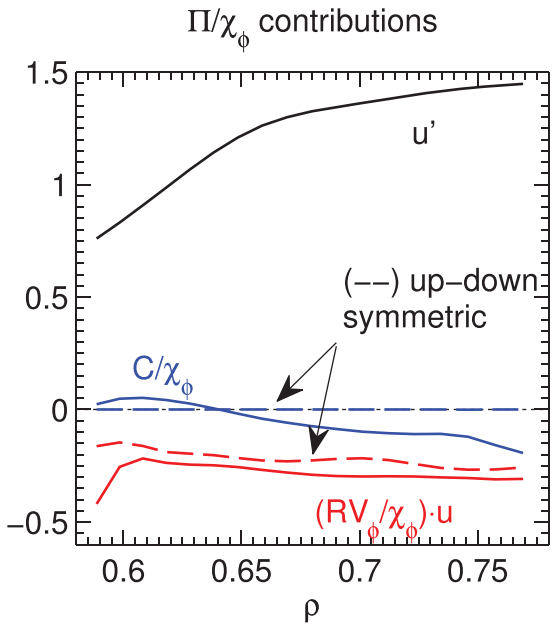

Figure 14. Predicted contributions to the normalized momentum flux, $\hat{\Pi}_\varphi = \hat{\chi}_\varphi\,[u' + (RV_\varphi/\chi_\varphi)u + \hat{C}_{\mathrm{UD}}/\hat{\chi}_\varphi]$, from the local, quasi-linear gyrokinetic simulations ($k_\theta\rho_s = 0.4$). Solid lines use the EFIT++ equilibrium surface as represented by a Fourier expansion [48]. The dashed lines represent the same surfaces but with the up-down asymmetric Fourier components set to zero.

Acknowledgment

The authors would like to thank J Hillesheim, A Kirk, and Y Q Liu, for useful discussions, J-K Park for the IPEC calculations, and W G would like to thank the MAST team for supporting this experiment. This work is supported by US DOE contract DE-AC02-09CH11466, and was (part-)funded by the RCUK Energy Programme (under grant EP/I501045) and the European Communities under the contract of Association between EURATOM and CCFE. To obtain further information on the data and models underlying this paper please contact PublicationsManager@ccfe.ac.uk. The views and opinions expressed herein do not necessarily reflect those of the European Commission.

References

[1] Shimada M. *et al* 2007 *Nucl. Fusion* **47** S1
[2] Peeters A.G. *et al* 2011 *Nucl. Fusion* **51** 094027
[3] Ida K. and Rice J.E. 2014 *Nucl. Fusion* **54** 045001
[4] Diamond P.H. 2013 *Nucl. Fusion* **53** 104019
[5] Mattor N. and Diamond P.H. 1988 *Phys. Fluids* **31** 1180
[6] Yoshida M. *et al* and the ITPA Transport & Confinement Topical Group 2012 *Nucl. Fusion* **52** 123005
[7] Peeters A.G., Angioni C. and Strinzi D. 2007 *Phys. Rev. Lett.* **98** 265003
[8] Peeters A.G., Strintzi D., Camenen Y., Angioni C., Casson F.J., Hornsby W.A. and Snodi A.P. 2009 *Phys. Plasmas* **16** 042310
[9] Peeters A.G., Angioni C., Camenen Y., Casson F.J., Hornsby W.A., Snodi A.P. and Strintzi D. 2009 *Phys. Plasmas* **16** 062311
[10] Hahm T.S., Diamond P.H., Gurcan O.D. and Rewoldt G. 2007 *Phys. Plasmas* **14** 072302
[11] Hahm T.S., Diamond P.H., Gurcan O.D. and Rewoldt G. 2008 *Phys. Plasmas* **15** 055902
[12] Hahm T.S., Lee J., Wang W.X., Diamond P.H., Choi G.J., Na D.H., Chung K.J. and Hwang Y.S. 2014 *Nucl. Fusion* **54** 123012
[13] Weisen H., Camenen Y., Salmi A., Versloot T.W., de Vries P.C., Maslov M., Tala T., Beurskens M., Giroud C. and JET-EFDA Contributors 2012 *Nucl. Fusion* **52** 042001
[14] Weisen H., Camenen Y., Salmi A., Versloot T.W., de Vries P.C., Maslov M., Tala T., Beurskens M., Giroud C. and JET-EFDA Contributors 2012 *Nucl. Fusion* **52** 114024
[15] Tala T. *et al* 2012 Tokamak experiments to study the parametric dependence of momentum transport *IAEA-FEC ITR/P1-19 (San Diego, CA)*
[16] Solomon W., Kaye S.M., Bell R.E., LeBlanc B.P., Menard J.E., Rewoldt G., Wang W., Levinton F.M., Yuh H. and Sabbagh S.A. 2008 *Phys. Rev. Lett.* **101** 065004
[17] Kaye S.M., Solomon W., Bell R.E., LeBlanc B.P., Levinton F., Menard J., Rewoldt G., Sabbagh S., Wang W. and Yuh H. 2009 *Nucl. Fusion* **49** 045010
[18] Solomon W.M. *et al* 2010 *Phys. Plasmas* **17** 056018
[19] Guttenfelder W., Kaye S.M., Ren Y., Solomon W., Bell R.E., Candy J., Gerhardt S.P., LeBlanc B.P. and Yuh H. 2016 *Phys. Plasmas* **23** 052508
[20] Guttenfelder W. *et al* 2013 *Nucl. Fusion* **53** 093022
[21] Guttenfelder W., Candy J., Kaye S.M., Nevins W.M., Wang E., Bell R.E., Hammett G.W., LeBlanc B.P., Mikkelsen D.R. and Yuh H. 2011 *Phys. Rev. Lett.* **106** 155004
[22] Guttenfelder W. *et al* 20120 *Phys. Plasmas* **19** 056119
[23] Doerk H., Jenko F., Pueschel M.J. and Hatch D.R. 2011 *Phys. Rev. Lett.* **106** 155003
[24] Doerk H., Jenko F., Görler T., Told D., Pueschel M.J. and Hatch D.R. 2012 *Phys. Plasmas* **19** 055907
[25] Kirk A. *et al* 2010 *Nucl. Fusion* **50** 034008
[26] Kirk A., Liu Y., Nardon E., Tamain P., Cahyna P., Chapman I., Denner P., Meyer H., Mordijck S., Temple D. and the MAST Team 2011 *Plasma Phys. Control. Fusion* **53** 065011
[27] Kirk A., Chapman I.T., Harrison J., Liu Y., Nardon E., Saarelma S., Scannell R. and Thornton A.J. 2013 *Plasma Phys. Control. Fusion* **55** 015006
[28] Lao L. *et al* 1985 *Nucl. Fusion* **25** 1611
[29] De Bock M.F.M., Conway N.J., Walsh M.J., Carolan P.G. and Hawkes N.C. 2008 *Rev. Sci. Instrum.* **79** 10F524
[30] Park J.-K., Boozer A.H. and Glasser A.H. 2007 *Phys. Plasmas* **14** 052110
[31] Shaing K.C., Ida K. and Sabbagh S.A. 2015 *Nucl. Fusion* **55** 125001
[32] Chapman I.T. *et al* and the MAST Team 2011 *Nucl. Fusion* **51** 073040
[33] Scannell R. 2010 *Rev. Sci. Instrum.* **81** 10D520
[34] Conway N.J., Carolan P.G., McCone J., Walsh M.J. and Wisse M. 2006 *Rev. Sci. Instrum.* **77** 10F131
[35] Hua M.-D., Chapman I.T., Field A.R., Hastie R.J., Pinches S.D. and the MAST Team 2010 *Plasma Phys. Control. Fusion* **52** 035009
[36] Chapman I.T., Hua M.-D., Pinches S.D., Akers R.J., Field A.R., Graves J.P., Hastie R.J., Michael C.A. and the MAST Team 2010 *Nucl. Fusion* **50** 045007
[37] Chapman I.T., Scannell R., Cooper W.A., Graves J.P., Hastie R.J., Naylor G. and Zocco A. 2010 *Phys. Rev. Lett.* **105** 255002
[38] Hawryluk R.J. 1981 An empirical approach to tokamak transport *Physics of Plasmas Close to Thermonuclear Conditions* vol 1, ed B. Coppi *et al* (Brussels: CEC) pp 19–46
[39] Pankin A., McCune D., Andre R., Batemann G. and Kritz A. 2004 *Comput. Phys. Commun.* **159** 157

[40] Goldston R.J. 1986 Basic physical processes of toroidal fusion plasmas *Proc. Course and Workshop (Varenna, 1985)* vol 1 (Brussels: CEC)
[41] Callen J.D., Cole A.J. and Hegna C.C. 2009 *Nucl. Fusion* **49** 085021
[42] Field A.R. *et al* 2004 *Proc. 20th IAEA FEC (Vilamoura, Portugal)* EXC/P2-11
[43] Field A.R., Michael C., Akers R.J., Candy J., Colyer G., Guttenfelder W., Ghim Y.-C., Roach C.M., Saarelma S. and the MAST Team 2011 *Nucl. Fusion* **51** 063006
[44] Houlberg W.A., Shaing K.C., Hirshman S.P. and Zarnstorff M.C. 1997 *Phys. Plasmas* **4** 3230
[45] Candy J. and Waltz R.E. 2003 *Phys. Rev. Lett.* **91** 045001
[46] Candy J. and Waltz R.E. 2003 *J. Comput. Phys.* **186** 545
[47] Candy J. and Belli E. 2010 *General Atomics Technical Report No.* GA-A26818
[48] Candy J. 2009 *Plasma Phys. Control. Fusion* **51** 105009
[49] Applegate D.J., Roach C.M., Connor J.W., Cowley S.C., Dorland W., Hastie R.J. and Joiner N. 2007 *Plasma Phys. Control. Fusion* **49** 1113
[50] Candy J., Waltz R.E., Fahey M.R. and Holland C. 2007 *Plasma Phys. Control. Fusion* **49** 1209
[51] Roach C.M. *et al* 2009 *Plasma Phys. Control. Fusion* **51** 124020
[52] Guttenfelder W. 2011 *J. Candy Phys. Plasmas* **18** 022506
[53] Howard N., Holland C., White A.E., Greenwald M. and Candy J. 2016 *Nucl. Fusion* **56** 014004
[54] Belli E.A. and Candy J. 2010 *Phys. Plasmas* **17** 112314
[55] Kluy N., Angioni C., Camenen Y. and Peeters A.G. 2009 *Phys. Plasmas* **16** 122302
[56] Hein T., Angioni C., Fable E., Candy J. and Peeters A.G. 2011 *Phys. Plasmas* **18** 072503
[57] Dominguez R.R. and Staebler G.M. 1993 *Phys. Fluids* B **5** 3876
[58] Casson F., Peeters A.G., Camenen Y., Hornsby W.A., Snodin A.P., Strintzi D. and Szepesi G. 2009 *Phys. Plasmas* **16** 0920303
[59] Camenen Y., Peeters A.G., Angioni C., Casson F.J., Hornsby W.A., Snodin A.P. and Strintzi D. 2009 *Phys. Rev. Lett.* **102** 125001
[60] Camenen Y. *et al* 2010 *Phys. Rev. Lett.* **105** 135003
[61] Buchholz R., Grosshauser S., Guttenfelder W., Hornsby W.A., Migliano P., Peeters A.G. and Strintzi D. 2015 *Phys. Plasmas* **22** 082307
[62] Camenen Y., Idomura Y., Jolliet S. and Peeters A.G. 2011 *Nucl. Fusion* **51** 073039
[63] Waltz R.E., Staebler G.M. and Solomon W.M. 2010 *Phys. Plasmas* **18** 042504
[64] Gurcan Ö.D., Diamond P.H., Hennequin P., McDevitt C.J., Garbet X. and Bourdelle C. 2010 *Phys. Plasmas* **17** 112309
[65] Wang W., Diamond P.H., Hahm T.S., Ethier S., Rewoldt G. and Tang W.M. 2010 *Phys. Plasmas* **17** 072511
[66] Wang W., Grierson B.A., Ethier S., Chen J., Startsev E., Diamond P.H. and Lu Z.X. 2016 *Proc. 26th IAEA FEC (Kyoto, Japan)* TH/P3-12
[67] Saarelma S., Hill P., Bottino A., Colyer G., Field G., McMillan B., Peeters A., Roach C.M. and the MAST Team 2012 *Plasma Phys. Control. Fusion* **54** 085012
[68] Field A.R., Dunai D., Ghim Y.-C., Hill P., McMillan B., Roach C.M., Saarelma S., Schekochihin A.A., Zoletnik S. and the MAST Team 2014 *Plasma Phys. Control. Fusion* **56** 025012
[69] Hillesheim J.C., Parra F.I., Barnes M., Crocker N.A., Meyer H., Peebles W.A., Scannell R., Thornton A. and the MAST Team 2015 *Nucl. Fusion* **55** 032003
[70] Parra F.I. and Catto P.J. 2010 *Plasma Phys. Control. Fusion* **52** 045005
[71] Barnes M., Parra F.I., Lee J.P., Belli E.A., Nave M.F.F. and White A.E. 2013 *Phys. Rev. Lett.* **111** 055005
[72] Guttenfelder W. *et al* 2016 Bulletin of the American Physical Society, GO6.4 *58th APS-DPP (San Jose, CA)*